

# Machine learning glass caging order parameters with an artificial nested neural network

Kaihua Zhang,<sup>1,\*</sup> Xinyang Li,<sup>2,3,\*</sup> Yuliang Jin,<sup>2,3,†</sup> and Ying Jiang<sup>1,4,‡</sup>

<sup>1</sup>*School of Chemistry, Beihang University, Beijing 100191, China*

<sup>2</sup>*CAS Key Laboratory of Theoretical Physics, Institute of Theoretical Physics, Chinese Academy of Sciences, Beijing 100190, China*

<sup>3</sup>*School of Physical Sciences, University of Chinese Academy of Sciences, Beijing 100049, China*

<sup>4</sup>*Center of Soft Matter Physics and Its Applications, Beihang University, Beijing 100191, China*

Around a glass transition, the dynamics of a supercooled liquid dramatically slow down, exhibited by caging of particles, while the structural changes remain subtle. In alternative to recent machine learning studies searching for structural predictors of glassy dynamics, here we propose to learn directly particle caging features defined purely according to dynamics. We focus on three transitions in a simulated hard sphere glass model, the melting of ultra-stable glasses, the Gardner transition and the liquid to ordinary glass transition. Implementing the machine learning algorithm based on a two-level nested neural network, we attain not only proper caging order parameters for all three transitions, but also a phase classification for input samples. A finite-size scaling analysis of the phase classification results identifies the order of melting (first) and Gardner (second) transitions. A false positive is avoided, as the liquid to glass transition is indicated as a crossover, rather than a phase transition with a well-defined transition point. This study paves the way to a generic approach for learning dynamical features in glassy systems, with a minimum requirement of system-specific knowledge.

## I. INTRODUCTION

The essential idea of Landau theory is to define suitable order parameters for phase transitions; e.g., a liquid-to-crystal transition can be characterized by order parameters that quantify the corresponding crystal structure. However, the problem is more complicated for transitions in disordered systems, such as glasses. For instance, around the liquid to glass transition, the viscosity increases by more than ten orders of magnitude over a small range of temperatures [1], while both phases seem to remain “disordered”.

Great efforts have been devoted to finding a proper glass order parameter based on static configurations of particles [2–13]. Besides the physics approach, recently researchers have attempted to address the conundrum by taking advantage of the power of machine learning (ML) techniques in extracting hidden information from structural data. A parameter called “softness” was learned to predict structural flow defects and plasticity in amorphous solids [14–17]. Graph neural networks (GNN) were used to predict long-time dynamics from the graph structure of initial particle positions [18]. Inspired by the GNN method, new structural descriptors were designed by recursively incorporating averaged features from neighbour shells [19]. Unsupervised ML methods were also developed to identify different clusters of particles based on their static correlations [20, 21], or network representations that encode interatomic potentials [22, 23].

In parallel to the static approach of structural order parameters, alternatively, one can consider glass *caging order parameters* defined purely based on dynamics [24, 25]. Compared to structural order parameters, which are often system-specific, caging order parameters seem more generic. For example, in spin glasses, where dynamics are usually decoupled from structures, it is standard to define and analyze overlapping order parameters [26], which play a similar role as the caging order parameters in structural glasses [25]. The caging/overlapping order parameters are at the core of mean-field theories of glass transitions, including the mode-coupling theory [27, 28], the replica theory [24–26], and the random first-order phase transition theory [29, 30]. To this day, it remains unexplored whether caging order parameters can be identified by ML.

Inspired by mean-field glass theories, in this article we design a two-level nested neural network (NNN) to learn directly caging features in glasses. Such a dynamics-oriented ML strategy does not rely on any structures. Upon training the model to achieve a phase classification [31] by the second-level network, the front-connected networks at the first level autonomously extract the inherent features beneath the replicated input configurations, physically interpreted as caging order parameters. Applying a proper finite-size scaling analysis to the machine provided classifications can further identify the order of phase transitions, a method that, to our knowledge, was previously unavailable. We demonstrate the above abilities by applying our method to melting and Gardner transitions in ultra-stable hard sphere (HS) glasses. In addition, we show that dynamical crossovers (e.g., the liquid to glass transition) can be distinguished from true phase transitions within this framework.

\* Contributed equally to this work

† yuliangjin@mail.itp.ac.cn

‡ yjiang@buaa.edu.cn

## II. SYSTEM AND TRANSITIONS

We consider a polydisperse HS glass model (see Electronic Supplementary Information (ESI)<sup>†</sup> Sec. S1 for details) whose mode-coupling theory (MCT) transition temperature is at  $\hat{T}_{\text{MCT}} \approx 0.044$  [32] (or volume fraction  $\varphi_{\text{MCT}} \approx 0.594$ , in this study, we use reduced temperatures). Two kinds of glasses, ordinary and ultra-stable glasses, are numerically created. The ordinary glasses are prepared by a moderate compression rate  $\Gamma = 10^{-3}$  using molecular dynamics (MD) simulations, corresponding to a glass transition temperature  $\hat{T}_{\text{g}} \approx 0.047$  (or  $\varphi_{\text{g}} \approx 0.58$ ). The ultra-stable glasses with a glass transition temperature  $\hat{T}_{\text{g}} \approx 0.033$  (or  $\varphi_{\text{g}} \approx 0.63$ ) are generated by an efficient swap Monte Carlo algorithm [33] (see ESI<sup>†</sup> Sec. S2). We prepare about 2000 uncorrelated equilibrium configurations at  $\hat{T}_{\text{g}}$ , which are referred to as *samples* in the following. Except for the preparation of ultra-stable initial states, all other simulations are performed using pure MD without swap.

We study three transitions: (i) The melting of ultra-stable HS glasses at the melting temperature  $\hat{T}_{\text{m}}(\hat{T}_{\text{g}}) > \hat{T}_{\text{g}}$ , by decompression with  $\Gamma = -10^{-4}$  from the deep equilibrium states at  $\hat{T}_{\text{g}} \approx 0.033$ . Recent studies suggested that the discontinuous melting of ultra-stable glasses is a vestige of a hidden first-order phase transition taking place in two coupled replicas of the system [34, 35]. (ii) The Gardner transition in ultra-stable HS glasses at  $\hat{T}_{\text{G}}(\hat{T}_{\text{g}}) < \hat{T}_{\text{g}}$ , by compression with  $\Gamma = 10^{-4}$  from  $\hat{T}_{\text{g}} \approx 0.033$ . The Gardner transition is a second-order phase transition separating the *stable glass* (at  $\hat{T} > \hat{T}_{\text{G}}$ ) and the *marginally stable glass* (at  $\hat{T} < \hat{T}_{\text{G}}$ ) phases [25, 32, 36–38]. (iii) The liquid to ordinary glass transition around  $\hat{T}_{\text{g}} \approx 0.047$ , which is believed to be a dynamical crossover rather than a true phase transition.

## III. METHODS

### A. Caging order parameters

In the framework of replica glass theory [25], the three transitions considered in this study (the melting transition, the Gardner transition, and the liquid to glass transition) are all characterized by *caging order parameters*. Particles diffuse in the liquid phase, but in the glass phase, they are confined in cages formed by nearby particles. Thus the average cage size  $\Delta$  can be used as an order parameter to identify glass and melting transitions:  $\Delta$  is small and finite in glasses (if activations are neglected as in mean-field theories [25]), while in liquids,  $\Delta \rightarrow \infty$  in the thermodynamic limit.

The order parameter for the Gardner transition is much more complicated. In the marginally stable glass phase, particle cages split into multiple hierarchical sub-cages. According to the mean-field theory [25, 39], the two phases around a Gardner transition are distinguished by, not a single scalar, but a probability distribution function  $P(\Delta_i)$  of single-particle cage size  $\Delta_i$ . However, in three-dimensional systems, as shown in this paper and in Ref. [38], it is more practical to look at the distribution  $P(\chi_i)$  of single-particle caging susceptibility  $\chi_i$ , which displays single and double peaks in stable and marginal glasses respectively.

### B. Preparation of input data using the replica construction

Practically, the caging order parameters are measured using the replica construction (let us consider  $N_r$  replicas of the same sample) [24, 25, 32, 39]. The replicated configurations are sampled from a given distribution  $P(C)$  depending on the state of the system. In liquids,  $P(C)$  is the equilibrium distribution and  $C$  can be any microscopic state in the ensemble. In glasses, there are multiple meta-stable states  $\mathcal{C}_{\text{MS}}$ , and different samples may belong to different meta-stable states. Thus the replicas of a given sample should be constructed from the conditional probability distribution  $P(C|\mathcal{C}_{\text{MS}})$ , where  $\mathcal{C}_{\text{MS}}$  is the meta-stable state that the given sample belongs to. From a dynamical point of view, it means that the same particle from different replicas should be confined in the same cage, but it is allowed to vibrate freely inside the cage. The purpose of replica construction is to translate caging dynamics to a static distribution of replicas. With this setup, the properties of cages can be obtained by analyzing the ensemble of replicas.

The design of our input data and network architecture is inspired by the replica construction (see Fig. 1). While the original system has  $N$  particles, the replicated system consists of  $N$  “molecules” at  $\{\mathbf{R}_i\}$ , where  $i = 1 \dots N$ , and each molecule is formed by  $N_r$  replicated “atoms” at coordinates  $\mathbf{R}_i = \{\mathbf{r}_i^A\}$ , where  $A = 1 \dots N_r$  is the replica index. Note that the spatial distribution of atoms inside a

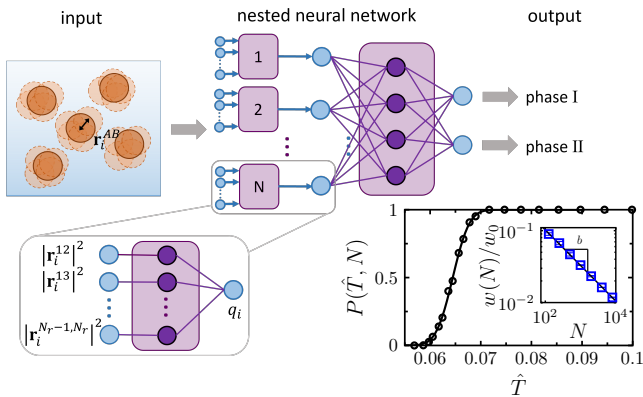


FIG. 1. Schematic diagram of the machine learning method. An example of the output  $P(\hat{T}, N)$  is shown for the melting transition ( $N = 125$ ), where the line represents the fitting to Eq. (1). (inset) Fitting the transition width  $w(N)$  to Eq. (3), giving  $b = 0.496(5)$ .

molecule represents dynamical rather than structural information: in the glass state, this distribution describes how the particle in the original unreplicated system vibrates in its cage. Although in principle the replica construction is equivalent to brute-force dynamical simulations, the former can facilitate the sampling, which is a significant advantage considering the slow dynamics in the glass state [32, 40].

In ML, it is conventional to perform additional treatment on the raw coordinate data  $\{\mathbf{R}_i\}$ ; without imposing inherent physical constraints, a necessary demand for big training data set would inevitably result in the inefficiency and inaccuracy in statistics [41]. We thus incorporate the translational and rotational symmetries of the physical system, and use as our input data the squared inter-atomic distances,  $\{|\mathbf{r}_i^{AB}|^2\}$ , where  $\mathbf{r}_i^{AB} = \mathbf{r}_i^A - \mathbf{r}_i^B$  (see Fig. 1). For the Gardner transition, we use the normalized quantity,  $\{u_{AB}^i\}$ , for the input, where  $u_{AB}^i = \frac{|\mathbf{r}_i^{AB}|^2}{\langle |\mathbf{r}_i^{AB}|^2 \rangle_r} - 1$ , with  $\langle \cdots \rangle_r$  representing the average over  $M_r = N_r(N_r - 1)/2$  pairs of replicas  $A$  and  $B$ . In short, for each sample, at a series of target temperatures  $\hat{T}$ , we prepare a one-dimensional array  $\{\mathbf{V}_i\}$  of  $M_r \times N$  elements as the input data to the neural network, where  $\mathbf{V}_i = \{|\mathbf{r}_i^{AB}|^2\}$  for melting and glass transitions, and  $\mathbf{V}_i = \{u_{AB}^i\}$  for the Gardner transition.

For each transition, we perform MD simulations to obtain  $N_s^{\text{total}}$  independent samples, and divide them into three non-overlapping data sets for the purposes of training ( $N_s^{\text{train}}$  samples), validation ( $N_s^{\text{valid}}$  samples) and prediction ( $N_s^{\text{pred}}$  samples), where  $N_s^{\text{total}} = N_s^{\text{train}} + N_s^{\text{valid}} + N_s^{\text{pred}}$ . Below we explain in detail how the input data to NNN are prepared, for the three types of transitions, accordingly.

### 1. Melting transition

The initial state of each sample is an equilibrium liquid configuration at  $\hat{T}_g = 0.033$ , generated by the swap algorithm. We then make  $N_r$  replicas of each sample, and decompress them using the Lubachevsky-Stillinger algorithm [42] with a negative compression rate  $\Gamma = -10^4$ , to  $N_{\hat{T}}$  different target temperatures in a window  $\hat{T} \in (0.033, 0.123)$ . The replicas share the same initial configuration at  $\hat{T}_g$ , but are assigned to different initial particle velocities drawn from the Maxwell-Boltzmann distribution. After decompression, the squared inter-atomic distances,  $\{|\mathbf{r}_i^{AB}|^2\}$ , are computed and used as the input to NNN. For the  $N_r$  replicas, there are in total  $M_r = N_r(N_r - 1)/2$  pairs can be formed,  $(A, B) = (1, 1), (1, 2), \dots, (N_r - 1, N_r)$ . The vector of  $\{|\mathbf{r}_i^{AB}|^2\} = \{|\mathbf{r}_i^{11}|^2, |\mathbf{r}_i^{12}|^2, \dots, |\mathbf{r}_i^{N_r-1, N_r}|^2\}$  is fed into the  $i^{\text{th}}$  small network at the first level (see Fig. 1). The complete input data is a vector of  $N \times M_r$  element,  $\{\{|\mathbf{r}_1^{AB}|^2\}, \{|\mathbf{r}_2^{AB}|^2\}, \dots, \{|\mathbf{r}_N^{AB}|^2\}\}$ . For the melting transition, we use  $N_s^{\text{total}} = 2400$ ,  $N_s^{\text{train}} = 1800$ ,  $N_s^{\text{valid}} = 300$ ,  $N_s^{\text{pred}} = 300$ , and  $N_{\hat{T}} = 35$ .

### 2. Gardner transition

The procedure is similar to the one for the melting transition, except that the compression rate  $\Gamma = 10^{-4}$  is positive. For the input data, instead of  $\{|\mathbf{r}_i^{AB}|^2\}$ , we use the normalized quantities  $\{u_{AB}^i = \frac{|\mathbf{r}_i^{AB}|^2}{\langle |\mathbf{r}_i^{AB}|^2 \rangle_r} - 1\}$ . It turns out that such a simple pre-treatment can efficiently improve the performance of our machine learning model (see ESI† Sec. S7). The following parameters are used:  $N_s^{\text{total}} = 2400$ ,  $N_s^{\text{train}} = 1800$ ,  $N_s^{\text{valid}} = 300$ ,  $N_s^{\text{pred}} = 300$ , and  $N_{\hat{T}} = 23$  (target  $\hat{T}$  is chosen in a window  $\hat{T} \in (0, 0.033)$ ).

### 3. Glass transition

The initial state of each sample is a dilute liquid configuration at  $\varphi = 0.2$ . Each sample is compressed to a target density  $\varphi$  (alternatively one can set a target temperature  $\hat{T}$ , or pressure  $\hat{P}$ ) with a fixed rate  $\Gamma$ , using the Lubachevsky-Stillinger algorithm. We choose in total  $N_{\hat{T}}$  different target densities in a window  $\hat{T} \in (0.002, 0.268)$ . Once the target  $\hat{T}$  is reached, we stop compression and make  $N_r$  replicas of each sample. These replicas share the same particle positions, but the particle velocities are independently reset according to the Maxwell-Boltzmann distribution. After making  $N_r$  replicas, we reset simulation time  $t$  to zero, and then perform constant volume ( $\Gamma = 0$ ) MD simulations. Note that the  $N_r$  replicas evolve independently because they are assigned to different velocities at  $t = 0$ . We then collect configurations of these replicas at  $t > 0$ , and compute  $\{|\mathbf{r}_i^{AB}|^2\}$ . For the data presented in this study, we have used  $\Gamma = 10^{-3}$ ,  $N_s^{\text{total}} = 1152$ ,  $N_s^{\text{train}} = 864$ ,  $N_s^{\text{valid}} = 144$ ,  $N_s^{\text{pred}} = 144$ , and  $N_{\hat{T}} = 29$ . Note that this procedure is different from the one explained above for melting and Gardner transitions: for the glass transition, the replicas are created after compression, while for melting and Gardner transitions, they are created before decompression/compression.

## C. Machine learning method

The structure of the input data and that of the two-level NNN are naturally matched. Each small network at the first level is responsible for a molecule, whose function is to map the input vector  $\mathbf{V}_i$  to a scalar  $q_i$ . Physically, the machine learned parameter  $q_i$  are intrinsically correlated to characteristic caging order parameters (see below). The mapping between the input data and the caging order parameter is independent of the choice of activation functions for both melting and Gardner transitions. The fully connected feed-forward neural network (FNN) at the next level takes  $\{q_i\}$  of the whole system as the input and makes a phase classification.

Note that the present algorithm can autonomously capture caging features from replicated configurations, and in the meanwhile realize the phase classification. It is thus prominently distinguished from the previous study on the Gardner transition [38], where the caging features were judiciously pre-designed as the input to, rather than provided as the output from, the ML algorithm.

For supervised phase classification, one needs to label samples prior to training [31]. This is realized by designing a *blanking window*  $[\hat{T}_2, \hat{T}_1]$ , out the range of which samples are labeled only; namely, we assign training samples at  $\hat{T} > \hat{T}_1$  to phase I and those at  $\hat{T} < \hat{T}_2$  to phase II. In principle, the results of our algorithm should not rely on the blanking window, fixed by hyperparameters  $\hat{T}_1$  and  $\hat{T}_2$  (ML results should not depend on hyperparameters); in other words, any predictions depending on such hyperparameters would be “unphysical” and need to be addressed with care (see below).

Once well trained, the algorithm makes a prediction of the probability  $P(\hat{T}, N)$  (or  $1 - P(\hat{T}, N)$ ) of a  $N$ -particle system belonging to phase I (or phase II), at any given temperature  $\hat{T}$ , calculated from test samples. The data are then fitted to an error function,

$$P(\hat{T}, N) = \frac{1}{2} + \frac{1}{2} \text{erf} \left\{ \left[ \hat{T} - \hat{T}_c(N) \right] / w(N) \right\}, \quad (1)$$

to estimate both the transition temperature  $\hat{T}_c(N)$  and the width  $w(N)$  of transition regime (see Fig. 1,  $\hat{T}_c = \hat{T}_m$ ,  $\hat{T}_G$  and  $\hat{T}_g^{\text{ML}}$  for melting, Gardner and glass transitions respectively). Additional details on the ML method is provided in ESI† Sec. S3.

#### D. Finite-size analysis method

To determine the order of phase transition, we perform a finite-size scaling analysis to the ML output [31, 38],

$$P(\hat{T}, N) = \mathcal{P} \left( |\hat{T} - \hat{T}_c| N^b \right). \quad (2)$$

Here (i)  $b = 1$  for a standard first-order phase transition without disorder, (ii)  $b = 1/2$  for a first-order phase transition with disorder, and (iii)  $b = 1/d\nu$  for a second-order phase transition. In addition,  $d = 3$  is the dimensionality and  $\nu$  the critical exponent for the divergence of correlation length. In general, the value of  $b = 1/d\nu$  in (iii) does not equal to 1 or 1/2, and thus by measuring  $b$ , one can distinguish between the above-mentioned three kinds of phase transitions. In practice,  $b$  is estimated by fitting the transition width data  $w(N)$  to,

$$w(N) = w_0 N^{-b}, \quad (3)$$

which can be derived from Eq. (2) ( $w_0$  is a constant prefactor, see Fig. 1).

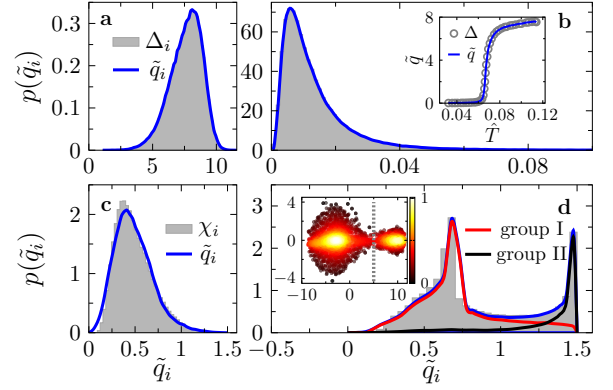


FIG. 2. Learning caging order parameters in (a-b) melting and (c-d) Gardner transitions ( $N = 125$  particles). For the melting transition, the two distributions  $P(\Delta_i)$  and  $P(\tilde{q}_i)$  nearly coincide in both (a) liquid ( $\hat{T} = 0.13$ ) and (b) glass ( $\hat{T} = 0.03$ ) phases. The Pearson correlation coefficient between  $\Delta_i$  and  $q_i$  is  $r = 1.0$  in both cases. (b-inset) Averaged  $\Delta(\hat{T})$  and  $\tilde{q}(\hat{T})$  around melting. For the Gardner transition, the distributions  $P(\chi_i)$  and  $P(\tilde{q}_i)$  are plotted in (c) the stable glass phase ( $\hat{T} = 0.03$ ) and (d) the marginally stable glass phase ( $\hat{T} = 10^{-5}$ ), with  $r = 0.96$  and  $r = 0.99$  respectively. (d-inset) Two groups of samples in the marginal phase visualized by the t-SNE method, where each point represents a sample and the color bar indicates normalized density of data points. The vertical dashed line indicates the estimated boundary between two groups, whose  $P(\tilde{q}_i)$  are plotted in the main panel.

## IV. RESULTS

### A. Melting transition

We first apply our method to the melting of ultra-stable glasses. We find that, once well trained, the machine learned parameter  $q_i$  is perfectly correlated to the physically defined caging order parameter  $\Delta_i = \langle |\mathbf{r}_i^A - \mathbf{r}_i^B|^2 \rangle_r$ , which characterizes the cage size of particle  $i$  [25, 32, 40] (see Fig. 2(a-b) and Fig. 3). The calculated Pearson correlation coefficient,  $r \equiv \frac{\sum_i (q_i - \bar{q})(\Delta_i - \bar{\Delta})}{\sqrt{\sum_i (q_i - \bar{q})^2 \sum_i (\Delta_i - \bar{\Delta})^2}} = 1.0$ , independent of  $\hat{T}$ , where  $\bar{q} = \langle q_i \rangle_i$  and  $\bar{\Delta} = \langle \Delta_i \rangle_i$ , with  $\langle \dots \rangle_i$  and  $\overline{\dots}$  being averages over particles and samples. The two parameters can be quantitatively matched by a linear rescaling,  $\tilde{q}_i \equiv c_1 q_i - c_2$ , where  $c_1$  and  $c_2$  are constants for  $i$  and  $\hat{T}$  but dependent on the initial parameterization in each training (see Fig. 3). The agreement is demonstrated in Figs. 2(a-b) by comparing the distributions  $p(\tilde{q}_i)$  and  $p(\Delta_i)$ , both before and after melting, and the average values  $\tilde{q}(\hat{T})$  and  $\Delta(\hat{T})$  at any  $\hat{T}$ .

To determine the parameters  $c_1$  and  $c_2$ , we collect the pairs of  $q_i$  and  $\Delta_i$  of all  $N$  particles in  $N_s$  samples at  $N_{\hat{T}}$  different temperatures (covering both phases), and perform a linear fitting (see Fig. 3(a) for an example). We find that the values of  $c_1$  and  $c_2$  are non-deterministic,

but the agreement between the rescaled predictions and the physically defined caging order parameters is very robust (Fig. 3(b)). It implies that the evolution of caging order parameter is correctly captured by NNN, but it is unnecessary to fix the rescale parameters  $c_1$  and  $c_2$  for the purpose of phase classification.

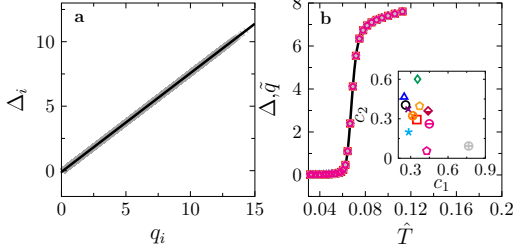


FIG. 3. Rescaling the predicted caging order parameters. (a) Determination of  $c_1$  and  $c_2$  for the melting transition. The data points of  $q_i$  and  $\Delta_i$  are collected from  $N = 125$  particles in  $N_s = 64152$  samples in the temperature window  $\hat{T} \in (0.033, 0.123)$ . The line represents the best fitting,  $\Delta_i = c_1 q_i - c_2$ , where  $c_1$  and  $c_2$  are  $\hat{T}$ -independent fitting parameters. With the fixed  $c_1$  and  $c_2$ , we define  $\tilde{q}_i \equiv c_1 q_i - c_2$ . (b) Comparison of the averaged prediction  $\tilde{q} = \frac{1}{N} \sum_i \tilde{q}_i$  (points) and the physical order parameter  $\Delta = \frac{1}{N} \sum_i \Delta_i$  (line), at different  $\hat{T}$  around melting. Note that  $c_1$  and  $c_2$  are fixed for each run of training, but vary for different runs (the initial values of network parameters are the same, but the training procedure is stochastic). We perform 12 independent runs, and plot the obtained  $c_1$  and  $c_2$  in the inset.

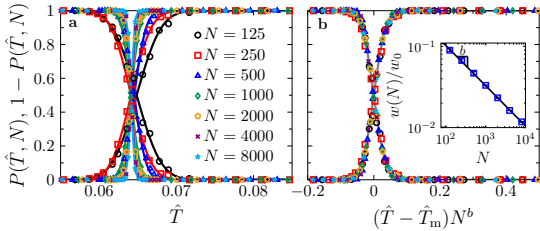


FIG. 4. Finite-size analysis of the machine learning results of the melting transition. (a) Machine learning results  $P(\hat{T}, N)$  and  $1 - P(\hat{T}, N)$  as functions of  $\hat{T}$  and (b)  $(\hat{T} - \hat{T}_m)N^b$ , where  $b = 0.496(5)$ . The data points are fitted to an error function (lines),  $P(\hat{T}, N) = \frac{1}{2} + \frac{1}{2} \text{erf} \left\{ \frac{[\hat{T} - \hat{T}_m(N)]}{w(N)} \right\}$ , where the transition temperature  $\hat{T}_m(N)$  (see Fig. 5(a)) and the width  $w(N)$  (see b-inset) are two fitting parameters. The exponent  $b = 0.496(5)$  is obtained by fitting the  $w(N)$  data to the scaling  $w(N) = w_0 N^{-b}$ . The data for the same  $N$  are represented by the same color in both panels.

The machine learning results  $P(\hat{T}, N)$  of the melting transition are fitted to Eq. (1), which gives the melting temperature  $\hat{T}_m(N)$  and the width of transition regime  $w(N)$  (see Fig. 4). The determined melting transition temperature  $\hat{T}_m \approx 0.064$  is consistent with the estimation from the peak of density fluctuation  $\chi_\varphi(\hat{T})$  (see

ESI† Fig. S2(a) and Fig. 5(a)). The transition width data  $w(N)$  are fitted to Eq. (3), giving  $b = 0.496(5)$ . The result  $b \simeq 1/2$  suggests that the melting of ultra-stable glasses is a first-order transition with disorder, consistent with the discontinuity on the equation of state (EOS)  $\hat{T}(\varphi)$  around  $\hat{T}$  (see Fig. S1 of ESI†). Note that  $b \simeq 1/2$  for the melting transition can be confirmed by the finite-size analysis of the physically-defined density susceptibility  $\chi_\varphi/N^a = \mathcal{X}(|\hat{T} - \hat{T}_c|N^b)$ , with an additional parameter  $a \approx 1$  (see ESI† Fig. S2(b)). This scaling function suggests the existence of two susceptibilities, a *disconnected* one,  $\chi_{\text{dis}} = \chi_\varphi \sim N^a \sim N$ , and a *connected* one  $\chi_{\text{con}} \sim d\mathcal{X}/d\hat{T} \sim N^b \sim N^{1/2}$ , related via,  $\chi_{\text{dis}} \sim \chi_{\text{con}}^2$ . Such a relationship seems to be ubiquitous in many transitions in disordered systems: it presents also around the critical point in the random field Ising model [43, 44], in the yielding of amorphous solids [45], and near the critical point in a replicated glass-forming model with coupling [35].

The output  $P(\hat{T}, N)$  represents the fraction of liquid samples identified by ML among the entire set of samples provided for prediction, for the given  $N$  and  $\hat{T}$ . Assuming that the system is self-averaging, i.e., a single large system is sufficient to represent the whole ensemble, one may also interpret  $P(\hat{T}, N)$  as the fraction of liquid-like particles in the sample. However, the inverse problem is not straight-forward (if not impossible), i.e., using a physical approach to find these liquid-like particles such that their probability is identical to  $P(\hat{T}, N)$ . Around the melting transition, it is not easy to define a sharp boundary between liquid-like and solid-like particles based on physical quantities such as the cage size. Furthermore, the property of self-averaging may break down in small systems with quenched disorder.

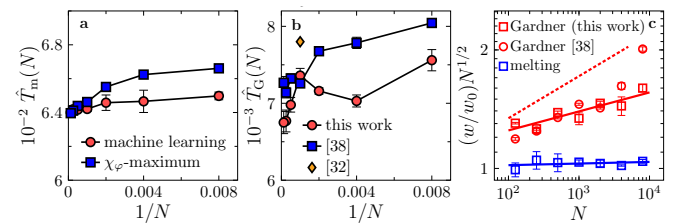


FIG. 5. Machine learned results of melting and Gardner transitions. (a) Melting temperature  $\hat{T}_m(N)$  of systems with different sizes  $N$ , obtained from ML and the maximum of density susceptibility  $\chi_\varphi$ . (b) Machine learned Gardner transition temperature  $\hat{T}_G(N)$  obtained in this work and in Ref. [38], as well as  $\hat{T}_G(N = 1000) \approx 0.0078$  by a physical method in Ref. [32]. (c) Finite-size scaling of machine learned transition width  $w(N)$  of both melting and Gardner transitions. The solid lines represent Eq. (3), where  $b = 1/2$  for the blue, and  $b = 1/\nu = 0.45(1)$  ( $\nu = 0.74(2)$ ) for the red. The red dashed line indicates the theoretical result  $\nu = 0.85$  [37]. Error bars represent the standard error of the mean in all figures.

## B. Gardner transition

Compared to the melting transition, the Gardner transition has much more subtle signatures – e.g., around the transition, the  $\hat{T}(\varphi)$  EOS does not display any jump or kink [32]. Figures 2(c-d) show that the machine learned  $q_i$  is highly correlated to the single particle caging susceptibility  $\chi_i \equiv \langle (u_i^{AB})^2 \rangle_r - \langle u_i^{AB} \rangle_r^2$  characterizing the fluctuation of cage size, i.e.,  $\tilde{q}_i \simeq \chi_i$ . The distribution  $p(\tilde{q}_i)$  shows a characteristic two-peak feature in the marginally stable phase ( $\hat{T} < \hat{T}_G$ ), similar to the behavior of  $p(\chi_i)$  observed previously [38]. The two peaks in  $p(\tilde{q}_i) \simeq p(\chi_i)$  demonstrate the existence of two dynamical caging modes in the marginally stable phase: particles with a larger/smaller  $\chi_i$  should have a more heterogeneous/homogeneous cage shape. This difference on single particle caging behavior is also reflected at the system level. Applying the unsupervised t-distributed stochastic neighbor embedding (t-SNE) method to  $\{\tilde{q}_i\}$ , we identify two groups of samples in the marginal phase, containing mostly heterogeneous/homogeneous caging particles respectively (see Fig. 2(d)). ML fails to identify the distribution of cage sizes  $p(\Delta_i)$ , suggested by the mean-field replica theory [25, 32, 36], as features for phase classifications (see Fig. S10 of ESI†), which shows the complexity of learning caging order parameters in finite dimensions.

The finite-size scaling of  $P(\hat{T}, N)$  and  $w(N)$  for the Gardner transition satisfy Eqs. (2) and (3) as well (see Fig. 6). The estimated transition temperature  $\hat{T}_G(N)$  is close to previously reported values by a physical approach [32] and ML using handcrafted descriptors [38] (see Fig. 5(b)).

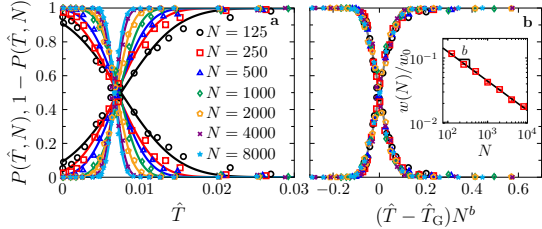


FIG. 6. Finite-size analysis of the Gardner transition. (a) Output from machine learning,  $P(\hat{T}, N)$  and  $1 - P(\hat{T}, N)$ , as functions of  $\hat{T}$  and (b)  $(\hat{T} - \hat{T}_G)N^b$ , for a few different  $N$ . The data points are fitted to an error function (lines),  $P(\hat{T}, N) = \frac{1}{2} + \frac{1}{2}\text{erf}\left\{\left[\frac{\hat{T} - \hat{T}_G(N)}{w(N)}\right]\right\}$ , where the transition temperature  $\hat{T}_G(N)$  (Fig. 5(b)) and the width  $w(N)$  (b-inset) are two fitting parameters. The exponent  $b = 1/d\nu = 0.45(1)$  is obtained by fitting the  $w(N)$  data to the scaling  $w(N) = w_0 N^{-b}$ .

Figure 5(c) emphasizes the difference on the finite-size scaling of  $w(N)$  in both melting and Gardner transitions. Such a plot can be used to identify the order of phase transitions: a first-order transition (melting) with disorder corresponds to  $b = 1/2$  in Eq. (3) and thus to a horizontal line in Fig. 5(c), while a second-

order transition (Gardner) should correspond to a line with a non-zero,  $\nu$ -dependent slope. The second-order nature of the Gardner transition is supported by the two-peak behavior of  $P(\chi_i)$  in Fig. 2(d), which is a universal feature of the probability distribution of order parameters below the critical temperature according to the Landau theory. Based on the relation  $b = 1/d\nu$ , we obtain the critical exponent  $\nu = 0.74(2)$ , close to the previous data,  $\nu = 0.78(2)$  from a ML numerical analysis [38] and  $\nu = 0.85$  from a field-theory calculation [37]. In addition, the method can be applied to standard first-order ( $b = 1$ ) and second-order phase transitions without disorder, such as those in the Ising model (see Sec. S5 of ESI†).

## C. Glass transition

Naturally, one could ask whether the above method can be applied to the liquid to ordinary glass transition. The difference between the two kinds of glasses, ordinary ( $\hat{T}_g \approx 0.047$ ) and ultra-stable ( $\hat{T}_g \approx 0.033$ ), is revealed by the hysteresis in their EOSs (see Fig 7(a)). Around  $\hat{T}_g$ , the average cage size  $\Delta$  of ordinary glasses depends strongly on the observation time  $t$  collapsed after compression, because particle hopping between cages is non-negligible (see ESI† Fig. S12). Nevertheless, for a fixed  $t$ , the evolution  $\Delta(\hat{T})$  can still be accurately captured by the machine learned  $\tilde{q}(\hat{T})$  (see Fig 7(b)).

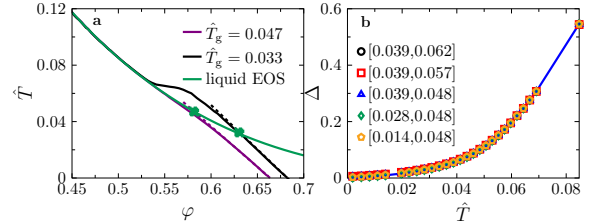


FIG. 7. Learning the caging order parameter of the glass transition. (a) EOSs for  $\hat{T}_g = 0.033$  and  $\hat{T}_g = 0.047$  ( $N = 500$ ). The glass transition temperature  $\hat{T}_g$  is practically defined as the intersection of the liquid EOS (green line) and the linearly fitted glass EOS (dashed line). (b) The average cage size  $\Delta$  (measured with  $t = 1$ ) as a function of  $\hat{T}$  (line), for ordinary glasses ( $\hat{T}_g = 0.047$ ), together with the machine learned  $\tilde{q}(\hat{T})$  using different blanking windows  $[\hat{T}_2, \hat{T}_1]$  (points).

Interestingly, the ML algorithm fails to identify a unique “transition point” (see Fig. 8). The estimated crossover temperature  $\hat{T}_g^{\text{ML}}$  relies on the labeling of two phases during training, i.e., the blanking window (see Fig. 9(c)). Figure 9(c) also shows that  $\hat{T}_g^{\text{ML}}$  is nearly identical to the center of blanking window,  $\hat{T}_{\text{center}}$ , suggesting that  $\hat{T}_g^{\text{ML}}$  simply separates low-density and high-density states, whose definitions are preset artificially by

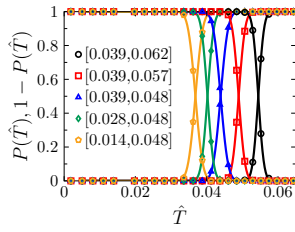


FIG. 8. Non-uniqueness of the glass transition point determined by machine learning. Output from machine learning,  $P(\hat{T})$  and  $1 - P(\hat{T})$ , as functions of  $\hat{T}$ , using a few different blanking windows (for  $N = 500$  systems,  $t = 1$ ). The data points are fitted to an error function (lines),  $P(\hat{T}) = \frac{1}{2} + \frac{1}{2} \text{erf} \left\{ \left[ \hat{T} - \hat{T}_g^{\text{ML}} \right] / w \right\}$ . The estimated  $\hat{T}_g^{\text{ML}}$  is plotted in Fig. 9(c).

the blanking window. In contrast, the estimated transition temperatures of melting and Gardner transitions are independent of such algorithm hyperparameters (see Figs. 9(a-b) and ESI† Figs. S9 and S11). Although the predicted  $P(\hat{T}, N)$  would look very similar for both dynamical crossovers and phase transitions (as the one plotted in Fig. 1), one should perform additional checks on the independence of hyperparameters (such as the blanking window discussed here) in order to confirm a true phase transition.

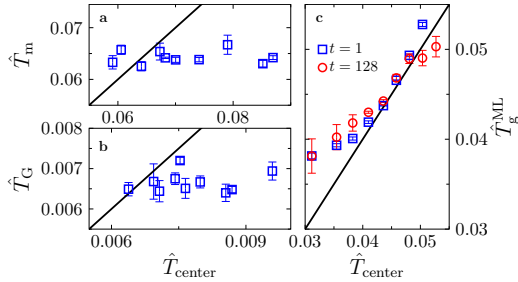


FIG. 9. Dependence of machine learned transition temperatures on the center of blanking window  $\hat{T}_{\text{center}}$ . (a) The melting temperature  $\hat{T}_m$  (data obtained for  $N = 2000$  systems) and (b) the Gardner transition temperature  $\hat{T}_G$  ( $N = 8000$ ) are independent of  $\hat{T}_{\text{center}}$ . (c) The crossover  $\hat{T}_g^{\text{ML}}$  from liquids to ordinary glasses is non-unique ( $N = 500$ , two different observation times  $t$ ). The solid lines represent  $y = x$ .

## V. CONCLUSION

We demonstrate that ML algorithm can identify caging features of glasses, based on which, phase classifications can be accomplished. In general, the input vector to the NNN,  $\mathbf{V}_i = \{v_i^1, v_i^2, \dots, v_i^{M_r}\}$ , represents a probability

distribution function  $p(v_i)$  describing certain features of particle  $i$ . The function of the front-connected small networks is to map the distribution  $p(v_i)$  to a scalar order parameter  $q_i$ , which can be either the mean (as in the case of melting and glass transitions) or the variance of  $p(v_i)$  (as in the case of Gardner transition). In ESI† Sec. S9, via a toy model, we further demonstrate that, the NNN can also identify  $q_i$  as the skewness (the third moment) of the input distribution, when the first two moments (mean and variance) do not carry useful information. Without loss of generality, we conclude that, in principle, the presented NNN method is capable of learning order parameters encoded in arbitrary-order statistical moments of the input data.

It would be challenging, if not impossible, to achieve similar classifications using only static information. The caging dynamics are directly related to the structure of phase space. In the language of replica theory, the breakdown of ergodicity in glasses is a result of replica symmetry breaking (RSB) [25]. The two-level structure of NNN can naturally capture caging order parameters of both the melting transition (1-step RSB) and the Gardner transition (full-step RSB). Increasing the number of nested levels would be useful for other types of RSB (e.g., 2-step RSB in glasses of bidisperse particles [46]). Finally, we expect generalizations of our method to other glassy systems, such as polymers and spin glasses.

## AUTHOR CONTRIBUTIONS

All authors contributed equally to the paper.

## CONFLICTS OF INTEREST

The authors declare no competing interests.

## ACKNOWLEDGEMENTS

Y. Jin acknowledges funding from National Natural Science Foundation of China (Project 11974361, Project 11935002, Project 12161141007, and Project 12047503), and Chinese Academy of Sciences (the Key Research Program of Frontier Sciences Grant NO. ZDBS-LY-7017, the Key Research Program Grant NO. XDPB15, and Grant NO. KGFZD-145-22-13). Y. Jiang acknowledges funding from Project 22073004 supported by National Natural Science Foundation of China. This work was granted access to the High-Performance Computing Cluster of Institute of Theoretical Physics - Chinese Academy of Sciences and Beihang University.

- 
- [1] C Austen Angell, “Formation of glasses from liquids and biopolymers,” *Science* **267**, 1924–1935 (1995).
  - [2] C Patrick Royall and Stephen R Williams, “The role of local structure in dynamical arrest,” *Physics Reports* **560**, 1–75 (2015).
  - [3] Hajime Tanaka, Hua Tong, Rui Shi, and John Russo, “Revealing key structural features hidden in liquids and glasses,” *Nature Reviews Physics* **1**, 333–348 (2019).
  - [4] Paul J Steinhardt, David R Nelson, and Marco Ronchetti, “Bond-orientational order in liquids and glasses,” *Physical Review B* **28**, 784 (1983).
  - [5] Chengjie Xia, Jindong Li, Yixin Cao, Binqian Kou, Xi-anhui Xiao, Kamel Fezzaa, Tiqiao Xiao, and Yujie Wang, “The structural origin of the hard-sphere glass transition in granular packing,” *Nature Communications* **6**, 1–9 (2015).
  - [6] Susana Marín-Aguilar, Henricus H Wensink, Giuseppe Foffi, and Frank Smallenburg, “Tetrahedrality dictates dynamics in hard sphere mixtures,” *Physical Review Letters* **124**, 208005 (2020).
  - [7] Mathieu Leocmach and Hajime Tanaka, “Roles of icosahedral and crystal-like order in the hard spheres glass transition,” *Nature Communications* **3**, 1–8 (2012).
  - [8] Akihiko Hirata, Pengfei Guan, Takeshi Fujita, Yoshihiko Hirotsu, Akihisa Inoue, Alain Reza Yavari, Toshio Sakurai, and Mingwei Chen, “Direct observation of local atomic order in a metallic glass,” *Nature Materials* **10**, 28–33 (2011).
  - [9] YC Hu, FX Li, MZ Li, HY Bai, and WH Wang, “Five-fold symmetry as indicator of dynamic arrest in metallic glass-forming liquids,” *Nature Communications* **6**, 1–8 (2015).
  - [10] Jade Taffs and C Patrick Royall, “The role of fivefold symmetry in suppressing crystallization,” *Nature Communications* **7**, 1–7 (2016).
  - [11] Hua Tong and Hajime Tanaka, “Revealing hidden structural order controlling both fast and slow glassy dynamics in supercooled liquids,” *Physical Review X* **8**, 011041 (2018).
  - [12] Hua Tong and Hajime Tanaka, “Structural order as a genuine control parameter of dynamics in simple glass formers,” *Nature Communications* **10**, 1–10 (2019).
  - [13] Daniel B Miracle, “A structural model for metallic glasses,” *Nature Materials* **3**, 697–702 (2004).
  - [14] Ekin D Cubuk, Samuel Stern Schoenholz, Jennifer M Rieser, Brad Dean Malone, Joerg Rottler, Douglas J Durian, Efthimios Kaxiras, and Andrea J Liu, “Identifying structural flow defects in disordered solids using machine-learning methods,” *Physical Review Letters* **114**, 108001 (2015).
  - [15] Samuel S Schoenholz, Ekin D Cubuk, Daniel M Sussman, Efthimios Kaxiras, and Andrea J Liu, “A structural approach to relaxation in glassy liquids,” *Nature Physics* **12**, 469–471 (2016).
  - [16] Ekin Dogus Cubuk, RJS Ivancic, Samuel S Schoenholz, DJ Strickland, Anindita Basu, ZS Davidson, Julien Fontaine, Jyo Lyn Hor, Y-R Huang, Y Jiang, *et al.*, “Structure-property relationships from universal signatures of plasticity in disordered solids,” *Science* **358**, 1033–1037 (2017).
  - [17] Samuel S Schoenholz, Ekin D Cubuk, Efthimios Kaxiras, and Andrea J Liu, “Relationship between local structure and relaxation in out-of-equilibrium glassy systems,” *Proceedings of the National Academy of Sciences* **114**, 263–267 (2017).
  - [18] Victor Bapst, Thomas Keck, A Grabska-Barwińska, Craig Donner, Ekin Dogus Cubuk, Samuel S Schoenholz, Annette Obika, Alexander WR Nelson, Trevor Back, Demis Hassabis, *et al.*, “Unveiling the predictive power of static structure in glassy systems,” *Nature Physics* **16**, 448–454 (2020).
  - [19] Emanuele Boattini, Frank Smallenburg, and Laura Filion, “Averaging local structure to predict the dynamic propensity in supercooled liquids,” *Phys. Rev. Lett.* **127**, 088007 (2021).
  - [20] Joris Paret, Robert L Jack, and Daniele Coslovich, “Assessing the structural heterogeneity of supercooled liquids through community inference,” *The Journal of Chemical Physics* **152**, 144502 (2020).
  - [21] Emanuele Boattini, Susana Marín-Aguilar, Saheli Mitra, Giuseppe Foffi, Frank Smallenburg, and Laura Filion, “Autonomously revealing hidden local structures in supercooled liquids,” *Nature Communications* **11**, 1–9 (2020).
  - [22] P Ronhovde, S Chakrabarty, D Hu, M Sahu, KK Sahu, KF Kelton, NA Mauro, and Z Nussinov, “Detecting hidden spatial and spatio-temporal structures in glasses and complex physical systems by multiresolution network clustering,” *The European Physical Journal E* **34**, 1–24 (2011).
  - [23] Peter Ronhovde, Saurish Chakrabarty, Dandan Hu, M Sahu, Kisor K Sahu, Kenneth F Kelton, Nicholas A Mauro, and Zohar Nussinov, “Detection of hidden structures for arbitrary scales in complex physical systems,” *Scientific reports* **2**, 1–6 (2012).
  - [24] Giorgio Parisi and Francesco Zamponi, “Mean-field theory of hard sphere glasses and jamming,” *Reviews of Modern Physics* **82**, 789 (2010).
  - [25] Giorgio Parisi, Pierfrancesco Urbani, and Francesco Zamponi, *Theory of Simple Glasses: Exact Solutions in Infinite Dimensions* (Cambridge University Press, 2020).
  - [26] Marc Mézard, Giorgio Parisi, and Miguel Virasoro, *Spin glass theory and beyond: An Introduction to the Replica Method and Its Applications*, Vol. 9 (World Scientific Publishing Company, 1987).
  - [27] Wolfgang Götze, *Complex dynamics of glass-forming liquids: A mode-coupling theory*, Vol. 143 (OUP Oxford, 2008).
  - [28] David R Reichman and Patrick Charbonneau, “Mode-coupling theory,” *Journal of Statistical Mechanics: Theory and Experiment* **2005**, P05013 (2005).
  - [29] TR Kirkpatrick and PG Wolynes, “Connections between some kinetic and equilibrium theories of the glass transition,” *Physical Review A* **35**, 3072 (1987).
  - [30] Theodore R Kirkpatrick, Devarajan Thirumalai, and Peter G Wolynes, “Scaling concepts for the dynamics of viscous liquids near an ideal glassy state,” *Physical Review A* **40**, 1045 (1989).
  - [31] Juan Carrasquilla and Roger G. Melko, “Machine learning phases of matter,” *Nature Physics* **13**, 431 (2017).

- [32] Ludovic Berthier, Patrick Charbonneau, Yuliang Jin, Giorgio Parisi, Beatriz Seoane, and Francesco Zamponi, “Growing timescales and lengthscales characterizing vibrations of amorphous solids,” *Proceedings of the National Academy of Sciences* **113**, 8397–8401 (2016).
- [33] Ludovic Berthier, Daniele Coslovich, Andrea Ninarello, and Misaki Ozawa, “Equilibrium sampling of hard spheres up to the jamming density and beyond,” *Physical Review Letters* **116**, 238002 (2016).
- [34] Robert L Jack and Ludovic Berthier, “The melting of stable glasses is governed by nucleation-and-growth dynamics,” *The Journal of Chemical Physics* **144**, 244506 (2016).
- [35] Ludovic Berthier and Robert L Jack, “Evidence for a disordered critical point in a glass-forming liquid,” *Physical Review Letters* **114**, 205701 (2015).
- [36] Patrick Charbonneau, Jorge Kurchan, Giorgio Parisi, Pierfrancesco Urbani, and Francesco Zamponi, “Frac-tal free energy landscapes in structural glasses,” *Nature Communications* **5**, 3725 (2014).
- [37] Patrick Charbonneau and Sho Yaida, “Nontrivial critical fixed point for replica-symmetry-breaking transitions,” *Physical Review Letters* **118**, 215701 (2017).
- [38] Huaping Li, Yuliang Jin, Ying Jiang, and Jeff ZY Chen, “Determining the nonequilibrium criticality of a gardner transition via a hybrid study of molecular simulations and machine learning,” *Proceedings of the National Academy of Sciences* **118**, e2017392118 (2021).
- [39] Patrick Charbonneau, Jorge Kurchan, Giorgio Parisi, Pierfrancesco Urbani, and Francesco Zamponi, “Glass and jamming transitions: From exact results to finite-dimensional descriptions,” *Annual Review of Condensed Matter Physics* **8**, 265–288 (2017).
- [40] Patrick Charbonneau, Yuliang Jin, Giorgio Parisi, Corrado Rainone, Beatriz Seoane, and Francesco Zamponi, “Numerical detection of the gardner transition in a mean-field glass former,” *Physical Review E* **92**, 012316 (2015).
- [41] Frank Noé, Alexandre Tkatchenko, Klaus-Robert Müller, and Cecilia Clementi, “Machine learning for molecular simulation,” *Annual review of physical chemistry* **71**, 361–390 (2020).
- [42] Boris D Lubachevsky and Frank H Stillinger, “Geometric properties of random disk packings,” *Journal of Statistical Physics* **60**, 561–583 (1990).
- [43] Michael Gofman, Joan Adler, Amnon Aharony, A Brooks Harris, and Moshe Schwartz, “Evidence for two exponent scaling in the random field ising model,” *Physical Review Letters* **71**, 1569 (1993).
- [44] Thomas Nattermann, “Theory of the random field ising model,” in *Spin glasses and random fields* (World Scientific, 1998) pp. 277–298.
- [45] Misaki Ozawa, Ludovic Berthier, Giulio Biroli, Alberto Rosso, and Gilles Tarjus, “Random critical point separates brittle and ductile yielding transitions in amorphous materials,” *Proceedings of the National Academy of Sciences* **115**, 6656–6661 (2018).
- [46] Harukuni Ikeda, Kunimasa Miyazaki, Hajime Yoshino, and Atushi Ikeda, “Multiple glass transitions and higher-order replica symmetry breaking of binary mixtures,” *Physical Review E* **103**, 022613 (2021).
- [47] Yuliang Jin, Pierfrancesco Urbani, Francesco Zamponi, and Hajime Yoshino, “A stability-reversibility map unifies elasticity, plasticity, yielding, and jamming in hard sphere glasses,” *Science Advances* **4**, eaat6387 (2018).
- [48] Yuliang Jin and Hajime Yoshino, “Exploring the complex free-energy landscape of the simplest glass by rheology,” *Nature Communications* **8**, 14935 (2017).
- [49] Beatriz Seoane and Francesco Zamponi, “Spin-glass-like aging in colloidal and granular glasses,” *Soft Matter* **14**, 5222–5234 (2018).
- [50] Tomáš Boublík, “Hard-sphere equation of state,” *The Journal of Chemical Physics* **53**, 471–472 (1970).
- [51] Stephen F Swallen, Katherine Traynor, Robert J McMahon, MD Ediger, and Thomas E Mates, “Stable glass transformation to supercooled liquid via surface-initiated growth front,” *Physical Review Letters* **102**, 065503 (2009).
- [52] Elisabeth Gardner, “Spin glasses with p-spin interactions,” *Nuclear Physics B* **257**, 747–765 (1985).
- [53] Qinyi Liao and Ludovic Berthier, “Hierarchical landscape of hard disk glasses,” *Physical Review X* **9**, 011049 (2019).
- [54] Antoine Seguin and Olivier Dauchot, “Experimental evidence of the gardner phase in a granular glass,” *Physical Review Letters* **117**, 228001 (2016).
- [55] Korbinian Geirhos, Peter Lunkenheimer, and Alois Loidl, “Johari-goldstein relaxation far below  $T_g$ : Experimental evidence for the gardner transition in structural glasses?” *Physical Review Letters* **120**, 085705 (2018).
- [56] Andrew P. Hammond and Eric I. Corwin, “Experimental observation of the marginal glass phase in a colloidal glass,” *Proceedings of the National Academy of Sciences* **117**, 5714–5718 (2020).
- [57] Monica Skoge, Aleksandar Donev, Frank H Stillinger, and Salvatore Torquato, “Packing hyperspheres in high-dimensional euclidean spaces,” *Physical Review E* **74**, 041127 (2006).
- [58] Dongkyu Kim and Dong-Hee Kim, “Smallest neural network to learn the ising criticality,” *Physical Review E* **98**, 022138 (2018).
- [59] Diederik P. Kingma and Jimmy Ba, “Adam: A method for stochastic optimization,” *International Conference on Learning Representations* (2015).
- [60] Nitish Srivastava, Geoffrey Hinton, Alex Krizhevsky, Ilya Sutskever, and Ruslan Salakhutdinov, “Dropout: a simple way to prevent neural networks from overfitting,” *The journal of Machine Learning Research* **15**, 1929–1958 (2014).
- [61] Laurens van der Maaten and Geoffrey Hinton, “Visualizing data using t-sne,” *Journal of Machine Learning Research* **9**, 2579–2605 (2008).
- [62] Kurt Binder, “Theory of first-order phase transitions,” *Reports on progress in physics* **50**, 783 (1987).
- [63] Martín Abadi, Paul Barham, Jianmin Chen, Zhifeng Chen, Andy Davis, Jeffrey Dean, Matthieu Devin, Sanjay Ghemawat, Geoffrey Irving, Michael Isard, *et al.*, “Tensorflow: A system for large-scale machine learning,” in *12th {USENIX} symposium on operating systems design and implementation ({OSDI} 16)* (2016) pp. 265–283.
- [64] M. E. J. Newman and G. T. Barkema, *Monte Carlo methods in statistical physics* (Clarendon Press, Oxford, 1999).
- [65] Lars Onsager, “Crystal statistics. i. a two-dimensional model with an order-disorder transition,” *Physical Review* **65**, 117 (1944).
- [66] Michael E Fisher and Robert J Burford, “Theory of critical-point scattering and correlations. i. the ising model,” *Physical Review* **156**, 583 (1967).

- [67] AL Talapov and HWJ Blöte, “The magnetization of the 3d ising model,” *Journal of Physics A: Mathematical and General* **29**, 5727 (1996).
- [68] Massimo Campostrini, Andrea Pelissetto, Paolo Rossi, and Ettore Vicari, “25th-order high-temperature expansion results for three-dimensional ising-like systems on the simple-cubic lattice,” *Physical Review E* **65**, 066127 (2002).
- [69] Rui Zhang, Bin Wei, Dong Zhang, Jia-Ji Zhu, and Kai Chang, “Few-shot machine learning in the three-dimensional ising model,” *Physical Review B* **99**, 094427 (2019).

# Supplementary Information

## S1. GLASS MODEL

The model [32, 33, 47–49] consists of  $N = 125 - 8000$  polydisperse hard spheres (HSs), whose diameters are distributed according to a continuous function  $P_D(D_{\min} \leq D \leq D_{\min}/0.45) \sim D^{-3}$ . The volume of simulation box is  $V$ , and periodic boundary conditions are used. The system state is characterized by volume fraction  $\varphi$  and reduced temperature  $\hat{T} = 1/\hat{P} = Nk_B T/PV$ , where  $P$  is the pressure,  $\hat{P}$  the reduced pressure,  $k_B = 1$  the Boltzmann constant, and  $T = 1$  the temperature. We set the mean diameter  $D_{\text{mean}}$  as unit length, and the particle mass  $m$  as unit mass. Crystallization is suppressed by polydispersity, and will not be discussed in this study.

The phase diagram of the model is presented in Fig. S1 [32]. Any state of the system is described by two thermodynamic parameters, the volume fraction  $\varphi$  and the reduced temperature  $\hat{T}$ . The Carnahan-Starling (CS) equation of state (EOS) [50] well captures the relationship between  $\varphi$  and  $\hat{T}$  of liquid states [32]. The mode-coupling theory (MCT) transition point,  $\hat{T}_{\text{MCT}} \approx 0.044$  (or  $\varphi_{\text{MCT}} \approx 0.594$ ), was estimated in [32], below which equilibrium becomes difficult in ordinary molecular dynamics (MD) simulations. Following convention, the intersection between liquid and glass EOSs is defined as the glass transition point  $\{\varphi_g, \hat{T}_g\}$ . The location of glass transition point depends on the compression rate  $\Gamma$ , and therefore, not unique. As can be seen in Fig. S1, the EOS of an ultra-stable glass ( $\hat{T}_g \ll \hat{T}_{\text{MCT}}$ ) displays enormous overshooting over the liquid EOS and the two EOSs are connected by an abrupt jump. In contrast, the EOS of a poorly annealed ordinary glass ( $\hat{T}_g \approx \hat{T}_{\text{MCT}}$ ) merges smoothly to the liquid one.

To study melting and Gardner transitions, we consider ultra-stable glasses. Deeply supercooled liquid states are prepared by using an efficient swap Monte Carlo (MC) algorithm [33]. Once the initial states are obtained, we switch to regular MD (without swap) to simulate follow-up dynamics. These deeply supercooled liquid states have extraordinarily large structural relaxation ( $\alpha$ -relaxation) time  $\tau_\alpha$  in the MD time unit, much larger than our MD simulation time window.

Two instabilities – the melting and the Gardner transitions – occur if one decompresses or compresses an ultra-stable HS glass. Under decompression, the glass is effectively “heated” up and eventually melts into a liquid at a melting temperature  $\hat{T}_m(\hat{T}_g) > \hat{T}_g$ . Although glass melting is a non-equilibrium procedure by definition, previous experiments [51] and simulations [34] showed that, this procedure in ultra-stable glasses is very similar to the melting of crystals, which is a first-order phase transition. In contrast, the melting of (poorly annealed) ordinary glasses is a smooth crossover without any discontinuous behavior.

On the other hand, a *Gardner transition* [36, 52] is

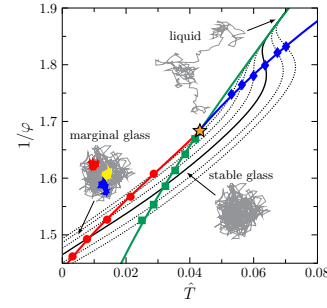


FIG. S1. Phase diagram of a hard sphere glass model [32]. The green, blue and red lines represent the CS liquid EOS, the melting line that separates liquid and glass phases, and the Gardner line that separates stable and marginally stable glass phases. The orange star represents the MCT transition point. The system is initially equilibrated at  $\hat{T}_g$  (green squares), and then evolves following the glass EOSs (dotted black lines) under compression or decompression. To study melting and Gardner transitions, we focus on the ultra-stable case of  $\hat{T}_g = 0.033$  (solid black line). Typical particle trajectories are plotted to show the diffusive motion in liquids, a confined cage in stable glasses, and the split of the cage into sub-cages in marginal glasses (the three sub-cages are visualized by trajectories of the same particle in three replicas, which are compressed from the same initial configuration at  $\hat{T}_g$ ).

expected to occur at  $\hat{T}_G(\hat{T}_g) < \hat{T}_g$  if an ultra-stable HS glass is compressed. The Gardner transition separates the *stable glass* (at  $\hat{T} > \hat{T}_G$ ) and the *marginally stable glass* (at  $\hat{T} < \hat{T}_G$ ) phases. It is predicted to be a second-order phase transition in large dimensions by the mean-field glass theory [25, 36]. Evidence of the Gardner transition in physical dimensions (2D and 3D) has been reported in a number of simulations [32, 48, 53] and experiments [54–56]. A fixed point is found by field-theory calculations, suggesting that the transition survives in low dimensions [37]. The existence of a Gardner transition in 3D ultra-stable HS glasses is supported by a recent numerical study, which combines finite-time-finite-size analyses with machine learning [38].

We do not study the melting and Gardner transitions in ordinary glasses: The melting of an ordinary glass is nearly reversible to the glass transition, and thus for our purpose, it is sufficient only to consider the latter. The Gardner transition in ordinary glasses is blurred by activated dynamics [32]; as a result, we do not expect to observe critical scalings.

## S2. MOLECULAR SIMULATION METHODS

### A. Molecular dynamics simulations

We use the Lubachevsky-Stillinger algorithm (event-driven MD) to simulate compression quench [42, 57]. During compression/decompression, the sizes of all

particles are increased/decreased proportionally with a fixed rate  $\Gamma = \frac{1}{2D} \frac{dD}{dt}$ . The simulation time is expressed in units of  $\sqrt{mD_{\text{mean}}^2/(k_B T)}$ . We simulate each configuration and measure its  $\hat{T}$  at a fixed packing fraction  $\varphi$ . Then we collect configurations at the desired  $\hat{T}$ , based on which physical quantities are computed. Additional simulation details can be found in Refs. [32, 38].

### B. Swap algorithm

The swap algorithm simulates artificial dynamics that can efficiently accelerate reaching equilibrium [33]. At each swap MC step, two particles are randomly picked, and swapped if they do not overlap with neighbor particles at the new positions. While the dynamics are unrealistic, the final configurations in equilibrium are equivalent to those generated by standard MD and MC simulations.

## S3. MACHINE LEARNING METHODS

### A. Architecture of the artificial neural network

The nested neural network (NNN) comprises two levels of networks, which in general can have different structures (see Fig. 1). There are  $N$  duplicated small networks at the first level, each of which extracts the latent caging features of one single particle. The small network has only one hidden layer, besides the input and output layers. Both input and hidden layers have  $M_r$  neuron nodes, and the output layer has a single node. The  $i^{\text{th}}$  hidden node is connected by a single link to the  $i^{\text{th}}$  input node, and is activated by the exponential linear unit (ELU) function. We have checked that the machine learning results do not change with a different type of activation function, such as a tanh function, for both melting and Gardner transitions. The output node simply takes an average of  $M_r$  hidden nodes. The  $N$  small networks share the same parameters (weights and bias), and thus there are only  $2M_r$  free parameters at the first level. The number of parameters can be further reduced from  $2M_r$  to 2, considering the permutation symmetry of replicas. In principle, one could choose other architectures (e.g., fully connected feed-forward neural network (FNN)) for small networks, and set their parameters to be independent. In practice, however, we find that using a small number of free parameters at the first level can significantly increase the efficiency of the NNN model during training, without losing its compatibility and predictive power. Generally, the number of free parameters can be minimized by considering the symmetries of the physical system under consideration, while networks with redundant parameters can work equally well if proper regularization is imposed [58].

The  $N$  output nodes of the first-level small networks

are considered as input nodes of the followed big FNN at the second-level. The FNN has one hidden layer of 128 nodes activated by ELU functions, and one output layer of two nodes that provide binary classifications through softmax activation functions.

### B. Blanking window

For the supervised learning of phases, we need to label in advance to which phase a given configuration belongs, during training and validation. A blanking window  $[\hat{T}_2, \hat{T}_1]$  is introduced to skip the vicinity of a (presumed) transition. Specifically, the following setup is used for the data presented in the main figures: for the melting transition, configurations at  $\hat{T} > \hat{T}_1 = 0.083$  and  $\hat{T} < \hat{T}_2 = 0.053$  are labeled as liquids and glasses respectively; for the Gardner transition, configurations at  $\hat{T} > \hat{T}_1 = 0.011$  and  $\hat{T} < \hat{T}_2 = 0.0045$  are labeled as stable and marginal glasses respectively. Note that, for both transitions, the machine learning results do not sensitively depend on the choice of blanking window (see Fig. 9, Secs. S6B and S7B). In contrast, the learning results of the glass transition correlates strongly to the blanking window.

### C. Training the nested neural network and validating predictions

A cross-entropy cost function is minimized during training. The Adam optimizer [59] is used to implement the stochastic gradient descent method for updating the network parameters. To avoid overfitting, a dropout strategy [60] is used, which randomly skips 20% hidden nodes at each step. To augment the training data set, we perform  $N_{\text{shuffle}} = 20 - 200$  random shuffles of the elements in the input vector, which is equivalent to randomly ordering particle indexes. In this way, we expand the training data set to  $N_s^{\text{train}} \times N_{\hat{T}} \times N_{\text{shuffle}} \sim 10^5$  samples. The random shuffling apparently destroys spatial correlations (if there is any) between particles. However, we find that it does not modify the final predictions noticeably. Validation is performed after each training step, by calculating the cost function for the validation data set. The entire training procedure is terminated when the validation cost function reaches a minimum. Such an early stopping strategy can efficiently avoid overfitting.

### D. Making predictions using the nested neural network

Once well trained, the NNN can make phase predictions for the samples in the testing data set. For each test sample at a temperature  $\hat{T}$ , the NNN provides an output value of 0 or 1. The arithmetic mean of the output over all test samples gives an estimation of the probability  $P$

of the system belonging to a specific phase, and  $1 - P$  to the other.

To achieve a reliable prediction, we independently train our NNN for 10 times (runs) and calculate the mean and the statistical error of the predicted  $P$ . For each run,  $N_s^{\text{train}}$  training samples and  $N_s^{\text{pred}}$  prediction samples are randomly selected from  $N_s^{\text{total}}$  samples, and the remaining  $N_s^{\text{valid}}$  samples are used for validation.

### E. Unsupervised classification using t-distributed stochastic neighbor embedding

We utilize the unsupervised t-distributed stochastic neighbour embedding (t-SNE) method [61] to group samples in the Gardner phase. The input data are the machine detected caging parameter  $\{\tilde{q}_i\}$  of each sample, where  $i = 1, 2, \dots, N$ . The algorithm conducts a non-linear dimensionality reduction, which maps each vector  $\{\tilde{q}_i\}$  to a point in two dimensions. In the two-dimensional space, data points are rearranged according to their similarities quantified by a t-distribution kernel function (see the inset of Fig. 2(d)).

## S4. FINITE-SIZE SCALING FUNCTION OF THE SUSCEPTIBILITY

To determine the order of phase transition, a standard way is to apply a finite-size analysis of data obtained from experiments or simulations. For example, the fluctuation of order parameter, or the susceptibility,  $\chi$ , follows a finite-size scaling function around a phase transition,

$$\chi/N^a = \mathcal{X}(|\hat{T} - \hat{T}_c|N^b), \quad (\text{S1})$$

where  $a, b$  are two exponents,  $\mathcal{X}(x)$  a scaling function whose concrete form is not important in our discussion, and  $\hat{T}_c$  the transition temperature. The values of  $a$  and  $b$  depend on the nature of transition: (i) For a standard first-order phase transition without disorder,  $a = 1$  and  $b = 1$  [62]. An example is the first-order phase transition between positive and negative ferromagnetic phases in the Ising model under an external field. (ii) For a first-order phase transition in the presence of disorder, such as the yielding transition [45] and the melting transition (see Fig. S2) in glasses,  $a = 1$  and  $b = 1/2$ . Equation (S1) then results in two susceptibilities, a *disconnected* one,  $\chi_{\text{dis}} = \chi \sim N^a \sim N$ , and a *connected* one  $\chi_{\text{con}} \sim d\mathcal{X}/d\hat{T} \sim N^b \sim N^{1/2}$ . The two susceptibilities are related via,  $\chi_{\text{dis}} \sim \chi_{\text{con}}^2$ , a relation found in the random field Ising model [43, 44]. (iii) For a second-order phase transition,  $a = b\gamma$  and  $b = 1/d\nu$ , where  $d$  is the dimensionality, and  $\gamma$  and  $\nu$  are the critical exponents for the divergences of susceptibility and correlation length. A standard example is the second-order phase transition between paramagnetic and ferromagnetic phases in the Ising model without a field.

Let us examine the finite-size scaling of the density susceptibility at fixed  $\hat{T}$ ,  $\chi_\varphi = N [\overline{\varphi^2} - (\overline{\varphi})^2] / (\overline{\varphi})^2$ , around the melting of ultra-stable glasses, where  $\overline{\dots}$  represents the average over samples. The density susceptibility displays a clear dependence on system size  $N$ , around the melting temperature  $\hat{T}_m \approx 0.064$  (see Fig. S2(a)). Its finite-size scaling satisfies Eq. (S1), with  $a \approx 1$  and  $b \approx 0.5$  (see Fig. S2(b)). The melting temperature  $\hat{T}_m(N)$  can be obtained from the peak position of  $\chi_\varphi(\hat{T})$  (data plotted in Fig. 5(a)). Note that the caging susceptibility around the Gardner transition suffers from strong finite-size and finite-time effects simultaneously, making a direct analysis difficult (see Ref. [38]).

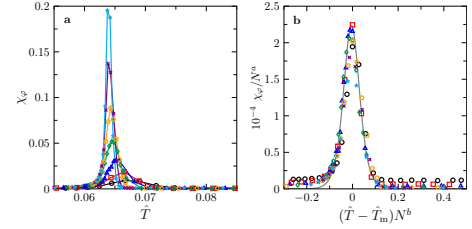


FIG. S2. Finite-size analysis of the density susceptibility around the melting transition. (a) Density susceptibility  $\chi_\varphi$  as a function of  $\hat{T}$ , for a few different system sizes  $N$ . (b) Collapse of the  $\chi_\varphi$  data according to Eq. (S1). Best collapsing is obtained by setting  $a = 0.8$ ,  $b = 0.5$  and  $\hat{T}_c = \hat{T}_m = 0.064$ .

## S5. MACHINE LEARNING PHASE TRANSITIONS IN THE ISING MODEL

### A. Machine learning algorithm

We study the Ising model in both two and three dimensions to validate the finite-size scaling function Eq. (2) in a standard equilibrium system. Machine learning is carried out using TensorFlow [63]. Following [31], we make use of a fully connected FNN, which comprises three layers (input, hidden and output) of nodes. The number of neurons in the input layer is equal to the number of spins  $N = L^d$ , where  $L$  is the linear size of the lattice and  $d$  is the dimensionality. The hidden layer is composed of 200 neurons activated by sigmoid functions, and the output layer has 2 neurons activated by a softmax function. During training, a cross-entropy cost function is minimized by means of a stochastic gradient descent method with an Adam optimizer [59]. In order to avoid overfitting, we adopt a dropout regularization [60], and an early stopping strategy.

The input data are spin configurations generated by the Wolff algorithm [64]. At a given magnetic field  $H$  and a given temperature  $T$ , we prepare  $N_s \approx 10,000$  samples, and use 80% of them for training, 10% for validation and 10% for prediction. Random shuffling is applied two to

four times to make sure that there are sufficient samples at each combination of  $(H, T)$  during training.

### B. Learning second-order phase transitions in two and three dimensions

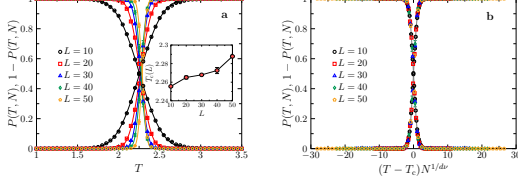


FIG. S3. Machine learning the second-order phase transition in the 2D Ising model. Output from machine learning,  $P(T, N)$  and  $1 - P(T, N)$ , as functions of (a)  $T$  and (b)  $(T - T_c)N^{1/d\nu}$ , for a few different  $N = L^2$  at  $H = 0$ . The data points are fitted to Eq. (S2) (lines), where the fitting parameters  $T_c$  and  $w$  are presented in the inset of (a) and Fig. (S7). The exponent  $b = 1/d\nu = 0.517(4)$  is obtained from fitting  $w(N) = w_0 N^{-b}$ , and is used in (b). Error bars represent the standard error of the mean in all figures.

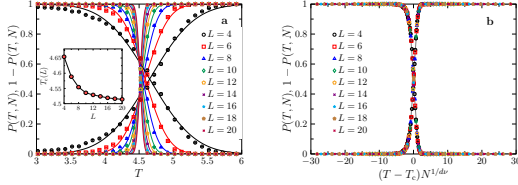


FIG. S4. Machine learning the second-order phase transition in the 3D Ising model. Output from machine learning,  $P(T, N)$  and  $1 - P(T, N)$ , as functions of (a)  $T$  and (b)  $(T - T_c)N^{1/d\nu}$ , for a few different  $N = L^3$  at  $H = 0$ , where  $b = 1/d\nu = 0.528(4)$ . The inset of (a) shows  $T_c(L)$ .

In two and three dimensions, a second order phase transition occurs at  $T_c$  when the temperature is varied under the zero-field condition  $H = 0$ . Previous studies have established the values of  $T_c$  and  $\nu$  (the critical exponent for the divergence of correlation length):  $T_c = 2.26918531421...$  [65] and  $\nu = 1$  [66] in 2D;  $T_c \approx 4.511528(6)$  [67] and  $\nu \approx 0.63012(16)$  [68] in 3D. Supervised machine learning techniques have been well utilized to learn the continuous phase transition in the Ising model in both 2D [31] and 3D [69]. Here we reproduce these results using our algorithm. For this purpose, we generate zero-field ( $H = 0$ ) input configurations around  $T_c$  at  $N_T$  different temperature points. The data points  $P(T, N)$  obtained from machine learning are fitted to

$$P(T, N) = \frac{1}{2} + \frac{1}{2} \text{erf} \{ [T - T_c(N)] / w(N) \}, \quad (\text{S2})$$

where  $N = L^d$ ,  $\text{erf}(x)$  is the error function, and  $T_c(N)$  and  $w(N)$  are two fitting parameters representing the

critical temperature and the width of transition region (see Fig. S3 for 2D and Fig. S4 for 3D). The estimated critical temperatures agree with existing values (see insets of Figs. S3 and S4). Next, we examine the finite-size scaling function Eq. (2). The scaling function suggests that,

$$w(N) \sim N^{-b}, \quad (\text{S3})$$

which is used to determine the critical exponent,  $\nu = 0.967(4)$  (or  $b = 1/d\nu = 0.517(4)$ ) in 2D and  $\nu = 0.631(3)$  (or  $b = 0.528(4)$ ) in 3D (see Fig. S7). These estimations are in a good agreement with the standard values,  $\nu = 1$  in 2D [66] and  $\nu \approx 0.63012$  in 3D [68]. Indeed, the data points of  $P(T, L)$  for different sizes can be collapsed onto a single curve if they are plotted as a function of the rescaled quantity  $(T - T_c)N^{1/d\nu}$  (see Figs. S3(b) and S4(b)).

### C. Learning first-order phase transitions in two and three dimensions

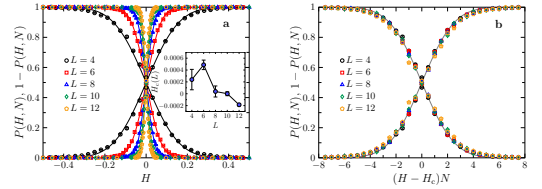


FIG. S5. Machine learning the first-order phase transition in the 2D Ising model. Output from machine learning,  $P(H, N)$  and  $1 - P(H, N)$ , as functions of (a)  $H$  and (b)  $(H - H_c)N$ , for a few different  $N = L^2$ . The inset of (a) shows  $H_c(L)$ .

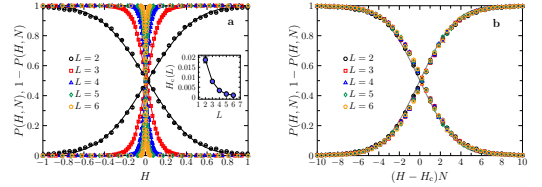


FIG. S6. Machine learning the first-order phase transition in the 3D Ising model. Output from machine learning,  $P(H, N)$  and  $1 - P(H, N)$ , as functions of (a)  $H$  and (b)  $(H - H_c)N$ , for a few different  $N = L^3$ . The inset of (a) shows  $H_c(L)$ .

For a fixed temperature  $T < T_c$ , a first-order phase transition occurs at  $H_c = 0$  when  $H$  is varied. To our knowledge, the finite-size scaling Eq. (2) of the first-order phase transition in the Ising model has not been systematically studied yet within the machine learning framework. In this study, we show that the expected scaling Eq. (2) is fully consistent with our data. We set  $k_B T/J = 2.1$  for the 2D model and  $k_B T/J = 4.0$  for the 3D model, where  $J$  is the interaction constant. Configurations are generated at  $N_H$  different external fields

around  $H_c = 0$ , with positive and negative fields evenly divided. The data points  $P(H, N)$  obtained from machine learning are fitted to

$$P(H, N) = \frac{1}{2} + \frac{1}{2} \text{erf} \{ [H - H_c(N)] / w(N) \}. \quad (\text{S4})$$

As shown in Figs. S5 and S6, the estimated transition field is close to  $H_c = 0$ . Furthermore, we obtain  $b \approx 0.96(2)$  for the 2D model, and  $b \approx 1.012(4)$  for the 3D model, which are consistent with the expected value  $b = 1$  [62].

#### D. Distinguishing between first- and second-order phase transitions

Based on above analyses, we confirm that, by utilizing the scaling function Eq. (2), the original machine learning approach proposed in [31] can be generalized to identify both first- and second-order phase transitions, in the standard Ising model. Very importantly, the order of phase transition can be identified because the finite-size exponents  $b$  in Eq. (2) are distinguishable within the numerical accuracy for first- and second-order phase transitions. As shown in Fig. S7,  $b = 1$  for first-order phase transitions (without considering the effect of disorder), and  $b = 1/d\nu$  for second-order phase transitions. While the phase transitions in the Ising model are in equilibrium, we show that the approach can be further generalized to non-equilibrium first-order (melting transition) and second-order (Gardner transition) phase transitions in disordered systems such as glasses (see Fig. 5).

### S6. ADDITIONAL RESULTS FOR THE MELTING TRANSITION

#### A. Dependence of the melting temperature on the decompression rate

The  $\hat{T} - \varphi$  EOSs of ultra-stable glasses in Fig. S8 show that the melting transition temperature  $\hat{T}_m$  decreases with slower decompression. It is expected that, in the limit  $\Gamma \rightarrow 0$ , the hysteresis in EOS will disappear and the glass melting will become a continuous crossover. However, for the range of  $\Gamma$  relevant to this study, the discontinuous feature remains. In the main text, we examine the finite-size effect for a fixed decompression rate  $\Gamma = -10^{-4}$ , and do not further discuss the rate-dependence.

#### B. Independence of learning results on the blanking window

During training, the samples at  $\hat{T} > \hat{T}_1$  and  $\hat{T} < \hat{T}_2$  are labeled as in the liquid and glass phases respectively. The samples in the blanking window  $[\hat{T}_2, \hat{T}_1]$  are

not used. Figure S9 shows that the machine predicted melting temperature  $\hat{T}_m$  and transition width  $w$  are independent of the blanking window (more specifically, the center of window  $\hat{T}_{\text{center}} = (\hat{T}_1 + \hat{T}_2)/2$  and the width of window  $\Delta\hat{T} = \hat{T}_1 - \hat{T}_2$ ). Note that, obviously we should require  $\hat{T}_m$  to be inside of the blanking window, i.e.,  $\hat{T}_2 < \hat{T}_m < \hat{T}_1$ . With this restriction, the choice of blanking window is flexible.

### S7. ADDITIONAL RESULTS FOR THE GARDNER TRANSITION

#### A. Choice of input data

According to the predictions from the mean-field glass theory [25, 39], the features of stable and marginally stable phases are encoded in  $\{\Delta_i\}$ , and thus in principle one should be able to use  $\{|\mathbf{r}_i^{AB}|^2\}$  as input data to train networks. However, in practice, the network fails to correctly identify both phases, when  $\{|\mathbf{r}_i^{AB}|^2\}$  are used as input. We find that (see Fig. S10), as  $\hat{T} \rightarrow 0$ , the predicted probability  $P \approx 0.5$ , while physically we expect  $P \approx 1$  (the samples should all belong to the marginally stable phase at sufficiently low  $\hat{T}$ ). On the other hand, correct and robust predictions are obtained when  $\{u_i^{AB} = \frac{|\mathbf{r}_i^{AB}|^2}{\Delta_i} - 1\}$  are used as input. Indeed, the cage size  $\Delta_i = \langle |\mathbf{r}_i^{AB}|^2 \rangle_r$  generally becomes smaller with decreasing  $\hat{T}$ , but this effect is independent of the physics of Gardner transition. The purpose of normalization is to remove this effect.

#### B. Independence of learning results on the blanking window

Figure S11 shows that the machine predicted Gardner transition temperature  $\hat{T}_G$  and the transition width  $w$  are independent of the choice of blanking window.

### S8. ADDITIONAL DYNAMICAL DATA FOR THE GLASS TRANSITION

In Fig. S12, we plot the data of mean-squared displacement (MSD),

$$\delta r^2(t) = \frac{1}{N} \sum_{i=1}^N |\mathbf{r}_i(t) - \mathbf{r}_i(0)|^2, \quad (\text{S5})$$

around the liquid to ordinary glass transition, where  $\mathbf{r}_i(0)$  is the position of particle  $i$  right after compression with a rate  $\Gamma = 10^{-3}$ , and  $\mathbf{r}_i(t)$  is the position at time  $t$  (we set  $t = 0$  and  $\Gamma = 0$  after compression). The dynamics clearly slow down with decreasing  $\hat{T}$ , but activated processes are non-negligible since the MSD is not completely

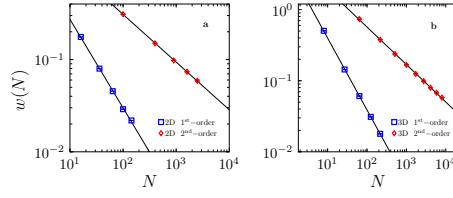


FIG. S7. Comparing the finite size scalings of first- and second-order phase transitions in the Ising model. The data of transition width  $w(N)$  are obtained from Figs. (S3-S6). The exponent  $b$  is obtained from fitting  $w(N) = w_0 N^{-b}$  (lines). (a) In the 2D Ising model, we obtain  $b = 0.96(2)$  for the first-order phase transition, and  $b = 1/d\nu = 0.517(4)$  (i.e.,  $\nu = 0.967(4)$ ) for the second-order phase transition. (b) In the 3D Ising model, we obtain  $b = 1.012(4)$  for the first-order phase transition, and  $b = 0.528(4)$  (i.e.,  $\nu = 0.631(3)$ ) for the second-order phase transition.

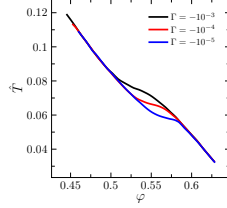


FIG. S8. Evolution of temperature  $\hat{T}$  as a function of volume fraction  $\varphi$  under decompression, for a few different decompression rate  $\Gamma$ . The system is composed of  $N = 125$  particles, and is decompressed from ultra-stable states at  $\{\varphi_g = 0.63, \hat{T}_g = 0.033\}$ . The liquid and glass EOSs are connected around the melting temperature  $\hat{T}_m$ , which decreases with slower decompression.

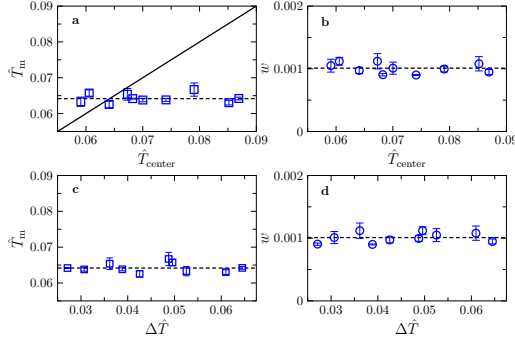


FIG. S9. Independence of  $\hat{T}_m$  and  $w$  on the blanking window  $[\hat{T}_2, \hat{T}_1]$ , for the melting transition. The two-level NNN is trained using a few different combinations of  $\hat{T}_1$  and  $\hat{T}_2$ , for  $N = 2000$  and  $\Gamma = 10^{-4}$ . The predicted  $\hat{T}_m$  and  $w$  are plotted as functions of  $\hat{T}_{\text{center}}$  and  $\Delta\hat{T}$ . The horizontal dashed lines are  $\hat{T}_m(N = 2000) = 0.064$  and  $w(N = 2000) = 0.001$  obtained for  $T_1 = 0.083$  and  $T_2 = 0.053$ . The solid line in (a) represents  $\hat{T}_m = \hat{T}_{\text{center}}$ . The same data in (a) are plotted in Fig. 9(a).

flat even at low  $\hat{T}$ . Figure S12(b) shows that the average cage size  $\Delta$  changes smoothly with  $\hat{T}$  and depends sensitively on the measurement time  $t$ . For a comparison, see the MSD of ultra-stable glasses in Fig. 2 of Ref. [32].

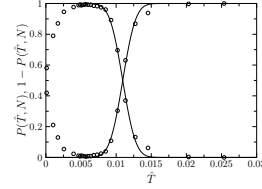


FIG. S10. Failure to learn the Gardner transition using  $\{|\mathbf{r}_i^{AB}|^2\}$  as input data. The test is performed for  $N = 2000$  systems.

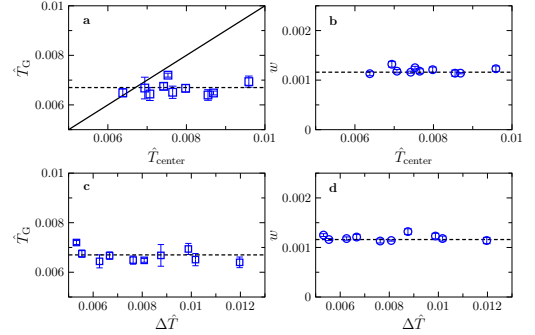


FIG. S11. Independence of  $\hat{T}_G$  and  $w$  on the blanking window  $[\hat{T}_2, \hat{T}_1]$ , for the Gardner transition. The predicted  $\hat{T}_G$  and  $w$  are plotted as function of  $\hat{T}_{\text{center}}$  and  $\Delta\hat{T}$  (for  $N = 8000$  systems). The horizontal dashed lines are  $\hat{T}_G(N = 8000) = 0.0067$  and  $w(N = 8000) = 0.0012$  obtained for  $T_1 = 0.011$  and  $T_2 = 0.0045$ . The solid line in (a) represents  $\hat{T}_G = \hat{T}_{\text{center}}$ . The same data in (a) are plotted in Fig. 9(b).

## S9. LEARNING A TOY MODEL

We artificially construct a toy model consisting of two phases, which are represented by two distribution functions respectively: a single Gaussian distribution  $p_I(x) = p_G(x; \mu, \sigma)$  for phase I, and a two-Gaussian distribution  $p_{II}(x) = \frac{1}{2}p_G(x; \mu_1, \sigma_1) + \frac{1}{2}p_G(x; \mu_2, \sigma_2)$  for phase II, where  $p_G(x; \mu, \sigma) = \frac{1}{\sigma\sqrt{2\pi}} e^{-\frac{(x-\mu)^2}{2\sigma^2}}$  is the standard Gaussian (normal) distribution of mean  $\mu$  and variance  $\sigma^2$ . We choose the parameters such that the means and variances are identical for the two distributions, but the skewnesses

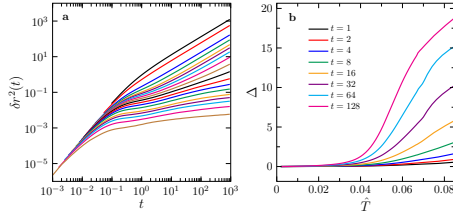


FIG. S12. Dynamical data of the glass transition. (a) MSD data at different densities ( $N = 500$ ): from top to bottom,  $\varphi = 0.3, 0.4, 0.5, 0.53, 0.55, 0.56, 0.57, 0.58, 0.59, 0.6, 0.61, 0.62, 0.63, 0.64, 0.645, 0.65, 0.655, 0.66$  ( $\hat{T} = 0.27, 0.16, 0.084, 0.069, 0.059, 0.054, 0.050, 0.045, 0.040, 0.036, 0.030, 0.025, 0.019, 0.014, 0.011, 0.0078, 0.0049, 0.0018$ ). (b) Average cage size  $\Delta$  as a function of  $\hat{T}$  for a few different measurement time  $t$ .

$\langle (\frac{x-\mu}{\sigma})^3 \rangle$  are different (see Table S1):  $\mu = 0, \sigma = 1.768$  in  $p_I(x)$ , and  $\mu_1 = -1, \sigma_1 = 2, \mu_2 = 1, \sigma_2 = 0.5$  in  $p_{II}(x)$ .

The setup for the machine learning algorithm is similar to that illustrated in Fig. 1. We use  $N = 1$  “particle”, whose feature is described by an input vector  $\mathbf{V}$  of  $M_r = 1000$  random numbers drawn from  $p_I(x)$  or  $p_{II}(x)$ . Thus  $\mathbf{V}$  is a representation of the probability distribution function for each phase. The front-connected small network maps the distribution  $p_I(x)$  or  $p_{II}(x)$  to a single scalar “order parameter”  $q$ . The two-level NNN is trained by  $N_s^{\text{train}} = 15000$  samples, and makes the phase prediction for  $N_s^{\text{pred}} = 2500$  samples. The rest of the method is equivalent to that for learning the glass model.

The Pearson correlation coefficients  $r$  between the first three moments and the parameter  $q$  are computed, taking account of both phases (see Table S1). The predicted  $q$  is strongly correlated to the skewness ( $r \approx 1$ ), while its correlation to the mean or the variance is negligible ( $r \approx 0$ ). This exercise shows that our method can correctly extract higher-order statistical moments from the input data when the mean and variance are trivial.

TABLE S1. Machine learning results for the toy model. Presented are the first three moments (mean, variance and skewness) of probability distribution functions  $p_I(x)$  and  $p_{II}(x)$ , and the Pearson correlation coefficient  $r$  between the moment and the parameter  $q$  learned by the small network.

	$p_I(x)$	$p_{II}(x)$	$r$
mean	0	0	-0.018
variance	3.125	3.125	0.109
skewness	0	-5.625	0.957